Ambient Noise Tomography with a Large Continental Seismic Array

Michael H. Ritzwoller, Fan-Chi Lin, Weisen Shen

Center for Imaging the Earth's Interior, Department of Physics, University of Colorado at Boulder, Boulder, CO 80309-0390 USA

Abstract

The emergence of large-scale arrays of seismometers across several continents presents the opportunity to image earth structure at unprecedented resolution, but methods must be created to exploit the capabilities of these deployments. The capabilities and limitations of a method called "eikonal tomography" applied to ambient noise data are discussed here. In this method, surface wave wavefronts are tracked across an array and the gradient of the travel time field produces estimates of phase slowness and propagation direction. Application is to data from more than 1000 stations from EarthScope USArray in the central and western US and new Rayleigh wave isotropic and anisotropic phase velocity maps are presented together with an isotropic and azimuthally anisotropic 3D Vs model of the crust and uppermost mantle. As a ray theoretic method, eikonal tomography models bent rays but not other wavefield complexities. We present evidence, based on the systematics of an observed 1ψ component of anisotropy that we interpret as anisotropic bias caused by wavefront healing, that finite frequency phenomena can be ignored in ambient noise tomography at periods shorter than ~40-50 sec. At longer periods a higher order term in the eikonal equation based on wavefront amplitudes or finite frequency sensitivity kernels must be introduced if the amplitude of isotropic anomalies and the amplitude and fast-axis direction of azimuthal anisotropy are to be determined accurately. We discuss how ambient noise data processing procedures will have to be modified to retain the higher order term in the eikonal equation and how ambient noise data can be used to compute empirical finite frequency kernels.

Submitted to *Comptes Rendus Geoscience*, September 1, 2010.

1. Introduction

The use of ambient noise to extract surface wave empirical Green's functions (EGFs) and to infer Rayleigh (e.g., Shapiro and Campillo, 2004; Sabra et al., 2005; Shapiro et al., 2005) and Love wave (Lin et al., 2008) group and phase speeds in continental areas is now well established. Phase and group velocity tomography to produce dispersion maps have been performed around the world (e.g., **US:** Bensen et al., 2008; Ekstrom et al., 2009; Moschetti et al., 2007; **Asia:** Kang and Shin, 2006; Cho et al., 2007; Fang et al., 2010; Li et al., 2009; Yang et al., 2010; Yao et al., 2006, 2009; Zheng et al., 2008; Zheng et al., 2010a; **Europe:** Yang et al., 2007; Villasenor et al., 2007; **New Zealand and Australia**: Arroucau et al., 2010; Lin et al., 2007; Saygin and Kennett, 2010; **Ocean bottom and islands:** Gudmundsson et al., 2007). Ambient noise tomography is typically performed at periods from about 8 sec to 40 sec, but the method has been applied successfully at global scales above 100 sec period (Nishida et al., 2009). It has also been used to obtain information about anelasticity (e.g., Prieto et al., 2009) and body wave (Roux et al., 2005; Gerstoft et al., 2008; Landes et al., 2010; Zhan et al., 2010) and overtone signals have also been recovered (e.g., Nishida et al., 2008). Numerous three-dimensional models of the crust and uppermost mantle have emerged from surface wave analyses for isotropic shear velocity structure (e.g., **US:** Bensen et al., 2009; Liang and Langston, 2008; Moschetti et al., 2010b; Stachnik et al., 2008; Yang et al., 2008b **Asia**: Guo et al., 2009; Nishida et al., 2008; Sun et al., 2010; Yao et al., 2008; Zheng et al., 2010b; **Europe**: Li et al., 2010; Stehly et al., 2009; **New Zealand and Australia**: Behr et al., 2010; **Ocean bottom and islands:** Brenguier et al., 2007; Harmon et al., 2007; **Africa:** Yang et al., 2008a), radial anisotropy (Moschetti et al., 2010a), and azimuthal anisotropy (e.g., Lin et al., 2010; Yao et al., 2010).

The rapid pace of these developments has been aided by the fact that once a surface wave EGF has been estimated by cross-correlating long time series of ambient noise recorded at a pair of stations, traditional methods of surface wave measurement, tomography, and inversion designed for application to earthquake records can be brought to bear on the result. These methods, however, largely have been developed to apply to observations obtained at single seismological stations. In this paper we discuss a new method to utilize

ambient noise within the context of a large-scale array such as the EarthScope USArray Transportable Array (Figure 1), temporary deployments of large numbers of seismometers such as PASSCAL and USArray Flexible Array experiments, and international analogs of the US efforts (e.g., the Virtual European Broadband Seismic Network, the rapidly growing seismic infrastructure in China sometimes referred to as ChinArray, and so on). Such extensive seismic arrays increasingly are becoming the preferred means to image high resolution earth structures, and new methods are needed to exploit their capabilities.

The ambient noise array methods that are discussed here still are based on the computation of EGFs between every pair of stations in the array and the measurement of inter-station phase travel times as a function of period (e.g., Bensen et al., 2007). Time domain (e.g., Bensen et al., 2007) and spatial autocorrelation (e.g., Ekstrom et al., 2009) methods yield similar travel time estimates (Tsai and Moschetti, 2010). However, for each target station, the set of EGFs to all other stations is used to compute the travel time field of the surface wavefield across a map encompassing the array. In this case, the eikonal equation (e.g., Shearer, 2009) can be used to estimate the wave slowness and apparent direction for every location on the map. At each location and frequency, measurements from different target stations can be combined to estimate the azimuthal dependence of the wave speed, which allows an estimate of isotropic and azimuthally anisotropic structures and rigorous uncertainties. We refer to this procedure as "eikonal tomography" (Lin et al., 2009) because of its basis in the eikonal equation. Eikonal tomography is described in section 2, as are results of its application to data from the EarthScope USarray across the western US. Examples of 3D Vs model results across the western US determined from ambient noise are contained in section 3.

There are several advantages of eikonal tomography compared with traditional tomographic methods (e.g., Barmin et al., 2001). Eikonal tomography accounts for ray bending but is not iterative, naturally generates uncertainties at each location in the tomographic maps, provides a direct (potentially visual) means to evaluate the azimuthal dependence of wave speeds, applies no ad hoc regularization because no inversion is performed, and is computationally very fast. There are approximations, however. The

method is based on 2D wave propagation stemming from its background in the 2D wave equation, goes on to discard a term from the equation that accounts for wavefront healing and other finite frequency effects, and the method is essentially ray theoretic. We present evidence in section 4 that discarding this term to derive the eikonal equation is justified at the periods where ambient noise tomography is typically performed (< 40 sec). We go on to show in section 5 that ambient noise measured across a large-scale array can be used to derive empirical finite frequency kernels that, in principle, can be applied tomographically. The theoretical background for many of the results presented here is described in greater detail by Lin et al. (2009), Lin and Ritzwoller (2010a,b), and Lin et al. (2010).

2. Eikonal Tomography

Shearer (2009) shows that from the 2D scalar wave equation, the modulus of the gradient of the wave travel time $T(\vec{x})$ is

$$\left|\nabla T\right|^2 = \frac{1}{c^2} + \frac{\nabla^2 A}{A\omega} \tag{1}$$

where $A(\vec{x})$ is position dependent wave amplitude, ω is wave frequency, and c is wave phase speed. At high frequencies, thus in the ray theoretic limit, the second term on the right side of equation (1) can be ignored, the local direction of ray propagation can be identified with the direction of the gradient term, and the eikonal equation can be written in vector form as

$$\nabla T = \frac{\hat{k}}{c} \tag{2}$$

where $\hat{k}$ is the unit vector in the direction of ray propagation. Lin et al. (2009) and others (e.g., Langston and Liang, 2008) show how equation (2) can be used tomographically. Justification for and the consequences of dropping the second term on the right in equation (1) are discussed in section 4.

The eikonal tomography method is based on computing the gradient of the observed travel time surfaces, $T(\vec{x})$, across a seismic array and is similar in many respects to other methods that track wavefronts (e.g. Langston and Liang, 2008; Pollitz, 2008). In so doing, estimates of the local wave slowness ($1/c$) and the direction of ray propagation emerge immediately from equation (2). An example for the 24 sec Rayleigh wave phase travel time surface across the western US centered on target station (USArray, Transportable Array) Q16A is shown in Figure 2. The local apparent phase speed (or "dynamic phase speed" after Wielandt, 1993) and ray direction inferred from the gradient of this travel time map is presented in Figure 3. Similar maps of phase speed and direction are derived from every other station in the array, which allows for the construction at each point across the map of plots of wave speed versus azimuth of propagation. The mean and the standard deviation of the mean of all phase speed measurements are used to estimate local isotropic phase speed c_0 and its uncertainty. To estimate azimuthal anisotropy for each location, all measurements from the nine nearby grid nodes with 0.6° separation (3×3 grid with target point at the centre) are combined to estimate the azimuthal variation of the phase speeds. This is shown for two locations in Figure 4 in which measured speeds are averaged in each 20° azimuthal bin and plotted as 1σ (standard deviation) error bars. These error bars derive from the scatter in the measurements across nine adjacent grid nodes and provide a rigorous estimate of the random component of uncertainty in the phase speed as a function of azimuthal angle ψ. Based on theoretical expectations for a weakly anisotropic medium (Smith and Dahlen, 1973) and the observation of 180° periodicity in the azimuthally dependent phase speed measurements (e.g. Figure 4), we fit, as a function of position and frequency, the following functional form to the observed variation of wave speed with azimuth

$$c(\psi) = c_0' + A\cos[2(\psi - \varphi)] \qquad (3)$$

where c_0' is the isotropic wave speed and A and φ are the amplitude and fast direction of the 2ψ anisotropy where the angle ψ is measured positive clockwise from north. Thus, at each point on the map (at each frequency) the quantities c_0', A, and φ are estimated together with their uncertainties. Note that c_0' and c_0 may differ slightly due to the nine point averaging where c_0' provides a lower uncertainty but also lower resolution estimate.

When measurements of phase slowness and propagation direction are taken simultaneously from all of the stations across USArray, much more stable results emerge than those that appear in Figure 3a. For example, the 24 sec Rayleigh wave isotropic phase speed map (c_0) is shown in Figure 5a and the amplitudes (A) and fast directions (φ) of the 2ψ component of anisotropy are shown in Figure 5b. Figure 5a and Figure 3a should be contrasted. No explicit smoothing or damping has been applied in constructing Figure 5b. The greater smoothness of Figure 5b compared with Figure 3a results from averaging all the measurements at each point (from different central stations) over azimuth. Spatial variations of the azimuthal anisotropy are also smooth and amplitudes typically rise only to several percent. Examples of uncertainties in the variables (c_0, A, and φ) are shown in map form for the 24 sec Rayleigh wave in Figure 6. All of these matters are described in greater detail by Lin et al. (2009).

3. Inversion for Isotropic and Azimuthally Anisotropic 3D Vs Models

Isotropic and azimuthally anisotropy dispersion maps and uncertainties, such as those shown in Figures 5 and 6, provide data to infer a 3D model of shear wave speeds within the earth. The vertical resolution and depth extent of the model will depend on the frequency band of the measurements. Ambient noise tomography typically produces maps down to periods of 6-8 sec, which means that structures in the shallow crust (top 5-10 km) can be resolved. Ambient noise tomography, however, rarely extends to periods above 30-40 sec at regional scales. The variation of the azimuthally dependent phase speed measurements increases dramatically at the longer periods. Thus, ambient noise alone constrains structures only to depths of 50-80 km. Deeper structures must be constrained with dispersion information from earthquakes as shown, for example, by Yang et al. (2008b), Moschetti et al. (2010a,b), and Lin et al. (2010).

Examples of Rayleigh wave phase speed maps from ambient noise at periods of 10 sec and 30 sec are shown in Figure 7. Some of the features revealed by these maps have been observed before and were discussed previously by Lin et al. (2008), Moschetti et al. (2010a,b), and Lin et al. (2010). But the maps in Figure 7 extend east of the Rocky Mountains, which now revieals new information about the transition from the tectonically

deformed western US to the stable mid-continent region. Comparison with similar maps constructed using teleseismic earthquakes, such as those shown in Figure 7c,f, has played an important role in justifying belief in the reliability of these maps, both for isotropic (e.g., Yang et al., 2008c) and azimuthally anisotropic variables. The 30 sec period isotropic Rayleigh wave speeds in Figures 7b (ambient noise) and 7c (earthquakes) differ on average by less than 0.1%, where the earthquake derived map is slightly faster, but the difference diminishes systematically as the number of earthquakes increases. The rms difference between these two isotropic maps is about 1%. The rms difference between the fast directions of azimuthal anisotropy determined from ambient noise and earthquakes for the 30 sec map is about 25° and the standard deviation of differences in the amplitude of anisotropy is about 0.6%.

At 10 sec period, several sedimentary basins clearly appear east of the Rocky Mountains: the Permian basin in west Texas, the Anadarko basin east of the Texas Panhandle, the Denver basin in eastern Colorado, the Powder River basin in Eastern Wyoming, and the Williston basin in western North Dakota. Although it is on average faster than the western US, the maps display significant variability in the Great Plains even at 30 sec period. Most of this variability at 30 sec period is due to variations in crustal structure and thickness, which heretofore has been poorly understood. Love wave maps also have been constructed (e.g., Lin et al., 2008; Moschetti et al., 2010a), but are not shown here.

Both linearized (e.g., Yang et al. 2008a,b) and Monte-Carlo (e.g., Shapiro and Ritzwoller, 2002; Moschetti et al., 2010a,b; Lin et al., 2010) methods to invert local Rayleigh and Love wave dispersion curves for a 3D Vs model are now well established. Example local dispersion curves for a point in northern Nevada are presented in Figure 8. These include the anisotropic dispersion curves (Fig. 8b, 8c) discussed by Lin et al. (2010). In these curves, below 25 sec period ambient noise measurements are used alone, between 25 sec and 45 sec period ambient noise and earthquake measurements are averaged, and above 45 sec period earthquake measurements are used alone. At this location and many others across the western US, measurements of Rayleigh wave anisotropic amplitude and fast direction differ between short and long periods. This indicates that anisotropy differs between the crust and uppermost mantle, but these curves can be fit by a model in which

crustal and uppermost mantle anisotropy are simple but distinct. Examples of crustal and uppermost mantle isotropic Vs wave speeds and azimuthal anisotropy are shown in Figure 9, which is discussed in detail by Lin et al. (2010). Uncertainty estimates in these model parameters derive from the Monte-Carlo inversion.

4. The Effect of Approximations

The derivation of the eikonal equation, equation (2), involves discarding the Laplacian term $\nabla^2 A / A\omega$. This may be justified by considering it to be a ray theoretic (high frequency) approximation, but may also be valid if the amplitude field would be sufficiently smooth; for example, if the length scale of the tomography is sufficiently large or isotropic structures are sufficiently smooth in the region. Thus, for global scale applications, rejection of this term may be justified. But, in ambient noise tomography, spatial length-scales are typically regional or local, not global. (This is also increasingly true in earthquake studies; e.g., Yang and Forsyth, 2006; Pollitz, 2008; Yang et al., 2008b). For this reason, in ambient noise tomography the validity of the rejection of the Laplacian term will dependent on the local smoothness of the medium and also will be frequency dependent.

To determine the relative size of the Laplacian term compared with the first (gradient) term on the right in equation (1), it would be best to compute it from amplitude observations just as the gradient term is computed from travel time observations. This is not so simple, however. In processing ambient noise (e.g., Bensen et al., 2007), amplitudes are typically normalized in the time domain by a running mean or one-bit normalization and spectra are commonly whitened. Thus, strictly speaking, amplitude information is lost. In addition, the amplitude of the ambient noise wavefield is neither isotropic nor stationary, but depends on excitation that varies with azimuth and season. Although, in principle, processing artifacts can be overcome or circumvented, doing so is beyond the scope of this paper.

The rejection of the Laplacian term, however, has an effect on apparent phase (or travel time) information that can be discerned in the observed azimuthal distribution of apparent phase speeds. Lin and Ritzwoller (2010b) discuss this in detail and show that discarding

this term introduces an apparent 1ψ bias in the azimuthal distribution of phase speeds in regions with strong lateral structural gradients. Their discussion is for earthquake waves, but the physical significance of the Laplacian term is the same for ambient noise wavefields. Thus, observation of a 1ψ term in the azimuthal distribution of phase speeds is evidence that the Laplacian term may be important for the fidelity of both the isotropic and anisotropic components of local phase velocity. Conversely, lack of observation of a 1ψ component is evidence that the Laplacian term and, thus, isotropic bias of inferred anisotropy is small and the use of the eikonal equation is justified.

Lin and Ritzwoller (2010b) discuss the physical cause of the 1ψ term, which we summarize briefly here. A wavefront that impinges upon a low velocity anomaly, for example, is indented during its propagation through the anomaly. After emerging from the anomaly, the wavefront heals according to Huygens' principle, a phenomenon that has been discussed previously by numerous researchers for regional scale surface wave tomography with earthquakes (e.g., Wielandt, 1993; Friederich and Wielandt, 1995; Yang and Forsyth, 2006; Bodin and Maupin, 2008; Pollitz, 2008). During healing, the apparent speed of the wave in the neighborhood of the indentation is raised relative to the physical speed of the medium of transport. This apparent increase in speed occurs where the wave emerges from the anomaly and the fast direction is in the direction of emergence. It does not appear where waves enter the anomaly. Thus, near the edge of a structural contrast, waves traveling in the opposite direction would have a different apparent phase speed and the azimuthal distribution of the apparent phase speed will be dominated by the 1ψ component. The details of the effect will depend on the shape of the anomaly, so smaller bias terms may also exist for the 0ψ, 2ψ, 3ψ, etc. components of local phase speed. To diagnose the presence of a 1ψ term, we modify equation (4) to include the term $A_{1\_psi}\cos[\psi - \alpha]$, where α is the fast direction and A_{1_psi} is the amplitude of the 1ψ component.

Figure 10 presents examples of the apparent distribution of phase speed as a function of azimuth for periods of 10 sec, 30 sec, and 60 sec at a point in northern Utah based on eikonal tomography with ambient noise measurements. At 10 sec and 30 sec period, only the 2ψ component is strong. However, at 60 sec period, in addition to larger error bars

due to the stronger scatter caused by lower signal-to-noise ratio at longer periods for ambient noise, the 1ψ component is dominant and is much stronger than the 2ψ component at any period. While lower signal-to-noise ratios at longer periods can prevent the extraction of meaningful 2ψ azimuthal anisotropy information, the existence of strong 1ψ signals is evidence for systematic bias in estimates of both isotropic and anisotropic variables. The size of the observed 1ψ component across the center of our study region, where we have measurements from all azimuths and isotropic structures are particularly complex, is shown in Figure 11 at several periods. The amplitude of this component is small at 10 sec and 30 sec period even though isotropic anomalies are strong. At 60 sec period, however, the 1ψ component has a large amplitude surrounding many of the prominent isotropic velocity anomalies (Fig. 11c,f). Around low velocity anomalies, such as the Snake River Plain anomaly seen in the 60 sec map in Figure 11c, the fast directions of the 1ψ component point radially outward from the isotropic anomaly. Around high velocity anomalies, such as that in Wyoming (Fig. 11c), the fast directions of the 1ψ component point radially inward toward the isotropic anomaly. This provides the diagnosis that the 1ψ signal arises from wavefront healing.

The observation of a gradual increase of the 1ψ component of Rayleigh wave phase velocities at periods above about 40 sec is evidence for systematic bias in estimates of isotropic and anisotropic structures. Thus, above 50 sec period, ignoring the Laplacian term in eikonal tomography is invalid in regions with strong lateral gradients in the isotropic wave speeds. Below 40 sec period, which is the focus of most ambient noise studies, the 1ψ term is largely negligible, even where structural gradients are exceptionally strong. The introduction of measurements obtained from earthquakes (e.g., Lin et al., 2010) helps to reduce uncertainties in the directionally dependent phase speed measurements and improves the azimuthal coverage particularly near the periphery of the map. It does not mitigate the wavefront healing effect at period above 50 sec, however (Lin and Ritzwoller, 2010b). It is possible and considerably easier to retain the Laplacian term in equation (1) for earthquake measurements, because of the loss of amplitude information in obtaining ambient noise measurements. Thus, in the context of regional scale structures such as those resolved in the western US, above 50 sec period the

Laplacian term in equation (1) should be retained to ensure the accuracy of the amplitude of isotropic structures and to minimize bias in the 2ψ component of azimuthal anisotropy.

5. Empirical Sensitivity Kernels

The wavefront healing that produces the spurious 1ψ signal in the azimuthal distribution of phase velocity is a finite frequency effect, meaning that it is a non-ray theoretic phenomenon that results from a wave's sensitivity to structures away from the ray path. As discussed in section 4, it can bias the estimated amplitude of isotropic structures as well as estimates of both the direction and amplitude of the 2ψ component of azimuthal anisotropy. One way to reduce this bias within eikonal tomography would be to retain the Laplacian term on the right side of equation (1). This is the approach taken by Lin and Ritzwoller (2010b) for earthquake waves, but it is complicated by the need to retain amplitude information in ambient noise data processing. Another approach would be to use finite frequency kernels in the tomographic inversion. Although the application of finite frequency kernels within eikonal tomography is not entirely clear, it is straightforward within the context of traditional tomographic algorithms (e.g., Barmin et al., 2001; Ritzwoller et al. 2002) that may be applied to ambient noise dispersion measurements. Although it has been the subject of considerable debate whether analytical kernels derived from 1D earth models are better than ad-hoc kernels or even ray theory (e.g., Yoshizawa and Kennett, 2002; van der Hilst and de Hoop, 2005; Montelli et al., 2006), theoretical and computational advances such as the adjoint method (e.g., Tromp et al., 2005) are now producing increasingly accurate sensitivity kernels from 2D and 3D models. The use of these numerical kernels in tomographic inversions has begun to appear (e.g., Peter et al., 2007, 2009; Tape et al., 2009). Nevertheless, the method remains computationally daunting, particularly for short period waves and when applied at very large scales, such as across the EarthScope USArray (Fig. 1) or other continental scale arrays.

Lin and Ritzwoller (2010a) present a new approach to the construction of finite frequency sensitivity kernels. They show that by mapping the phase travel time observed across a large seismic array (e.g., Fig. 2) and utilizing the virtual source property of ambient noise

cross-correlation measurements, the adjoint method can be applied to construct empirical sensitivity kernels within the array without numerical simulations. Because all phase travel times are measured via surface waves propagating on the earth, the empirical kernels represent the sensitivity of surface waves in which the real earth acts as the reference model. Example empirical finite frequency phase velocity kernels for the 20 sec and 40 sec period Rayleigh waves are shown in Figure 12 and contrasted with analytical 1D kernels.

Significant discrepancies exist between the empirical kernels and analytical kernels derived with a 1D earth model in regions with large lateral wave speed variations. Lin and Ritzwoller (2010a) show that more accurate travel time predictions (to second-order in model perturbations) can be achieved in such regions by averaging the analytical and empirical kernels than using the analytical kernel alone (first-order in model perturbations). In principle, with the use of the empirical sensitivity kernels in a tomographic inversion, single-scattering (finite frequency effects such as wavefront healing) and multiple-scattering effects (off-great-circle propagation) can be accounted for simultaneously in a computationally efficient framework.

6. Conclusions

The development and growth of dense, large-scale seismic continental arrays, such as deployments that are now in place in China, Europe, and the US (e.g., EarthScope USarray), present unprecedented opportunities to map the substructure of continents at resolutions that seemed impossible before their deployment within the last half decade. To capitalize on the investments that these and similar arrays represent, new methods of seismic tomography need to be developed to wring from the arrays more information, more reliable information, and qualitative and quantitative assessments of the accuracy of the information. We present here a discussion of one such method, called eikonal tomography, which is designed to exploit information contained in surface waves that compose ambient noise. We argue that the eikonal tomography method extracts information from ambient noise at high resolution about isotropic wave speeds as well as azimuthal anisotropy at periods from less than 10 sec to about 40 sec. The information at the short period end of this band often provides unique constraints on crustal structure as

surface waves below 20 sec period are difficult to observe in many locations with earthquake sources and teleseismic body wave do not determine crustal structures well. In addition, eikonal tomography provides meaningful uncertainty estimates about all measured quantities.

Perhaps the greatest challenge to face new methods designed to fully exploit the emerging continental arrays will be to mitigate the effects of complexities in the seismic wavefield on the inferred quantities. This is particularly true if relatively subtle influences on the wavefield, such as azimuthal anisotropy, are the intended inferred observable. In particular, wavepath bending or refraction, scattering and multipathing on the way to the array (for teleseismic earthquakes) which are often called non-planar wave effects, wavefield effects within the array (such as wavefront healing), and azimuthal variations in excitation of the wavefield all can affect the observed phase speed of the wavefield and introduce spurious or apparent effects unless they are accounted for explicitly in the data processing and inversion procedures.

Eikonal tomography explicitly tracks wavefields and, therefore, accounts for wavepath bending that is particularly important near sharp structural contrasts and at short periods. But, it is a ray theoretic method and, therefore, does not model structural or wavefield effects away from the ray. However, by its very nature, the inter-station ambient noise wavefield, in contrast with earthquakes, is free from effects external to the array. Wavefield complexities such as wavefront healing potentially are important for ambient noise, however, and eikonal tomography, defined by equation (2) here, does not explicitly account for it. We present evidence that below 40 sec period imaging methods based on ambient noise can ignore wavefield complexities, such as wavefront healing. Above ~50 sec period, however, they become increasingly important both for ambient niose and earthquake wavefields. In this case, eikonal tomography will need to be modified to include the second term in equation (1), which is based on the amplitude of the observed wavefield. This Laplacian term is deceptively simple, but it accounts for a wide array of wavefield effects, including wavefield complexities arising within the array (or outside the array for earthquake observations) as well as azimuthal variations in excitation. Its application, however, requires that amplitudes be well defined so that instruments must

be well calibrated and processing procedures cannot result in the degradation or loss of information about amplitudes.

The retention of the Laplacian term in equation (1) with earthquake data is relatively straightforward and is discussed by Lin and Ritzwoller (2010b). Standard ambient noise data processing, however, typically loses amplitude information. Therefore, to apply eikonal tomography above ~50 sec period and retain the Laplacian term in equation (1) will require that these procedures be modified so that, at the very least, the effects of data selection and of various normalizations in the time and frequency domain are understood and can be effectively undone. This is an area of active research.

Another approach to model non-ray theoretic effects is to employ empirical finite frequency sensitivity kernels. We discuss the construction of such kernels here and Lin and Ritzwoller (2010a) describes them in greater detail.

Acknowledgments: Instruments [data] used in this study were made available through EarthScope (www.earthscope.org; EAR-0323309), supported by the National Science Foundation. The facilities of the IRIS Data Management System, and specifically the IRIS Data Management Center, were used for access to waveform and metadata required in this study. The IRIS DMS is funded through the US National Science Foundation (NSF) and specifically the GEO Directorate through the Instrumentation and Facilities Program of the National Science Foundation under Cooperative Agreement EAR-0552316. This work has been supported by NSF grants EAR-0711526 and EAR-0844097.

References:

Arroucau, P., Rawlinson, N., Sambridge, M. New insight into Cainozoic sedimentary basins and Palaeozoic suture zones in southeast Australia from ambient noise surface wave tomography. *Geophys. Res. Lett.* **37**, L07303 (2010).

Barmin, M.P., Ritzwoller, M.H. & Levshin, A.L. A fast and reliable method for surface wave tomography, *Pure Appl. Geophys.* **158** (8), 1351 – 1375 (2001).

Behr, Y., Townend, J., Bannister, S., Savage, M. K. Shear velocity structure of the Northland Peninsula, New Zealand, inferred from ambient noise correlations. *J. Geophys. Res.-Solid Earth 115*, B05309 (2010).

Bensen, G. D. Ritzwoller, M. H., Barmin, M. P., Levshin, A. L., Lin, F., Moschetti, M. P., Shapiro, N. M. & Yang, Y. Processing seismic ambient noise data to obtain reliable broad-band surface wave dispersion measurements. *Geophys. J. Int.* **169**, 1239-1260 (2007).

Bensen, G. D., M. H. Ritzwoller & N. M. Shapiro. Broadband ambient noise surface wave tomography across the United States. *J. Geophys. Res.* ***113*** (B5), B05306, doi:10.1029/2007JB005248 (2008).

Bensen, G. D., M. H. Ritzwoller & Y. Yang. A 3-D shear velocity model of the crust and uppermost mantle beneath the United States from ambient seismic noise. *Geophys. J. Int.* **177,** 1177-1196 (2009).

Bodin, T. & Maupin, V. Resolution potential of surface wave phase velocity measurements at small arrays. *Geophys. J. Int.* **172**, 698-706 (2008).

Brenguier, F., Shapiro, N.M., Campillo, M., Nercessian, A., Ferrazzini, V. 3-D surface wave tomography of the Piton de la Fournaise volcano using seismic noise correlations. *Geophys. Res. Lett.* ***34*** (2), L02305 (2007).

Cho, K.H., Herrmann, R.B., Ammon, C.J., Lee, K. Imaging the upper crust of the Korean Peninsula by surface-wave tomography. *Bull. Seism. Soc. Am.,* **97** (1), 198-207 Part B Sp. Iss. S (2007).

Ekstrom, G., Abers, G.A., Webb, S.C. Determination of surface-wave phase velocities across USArray from noise and Aki's spectral formulation. *Geophys. Res. Lett.* **36**, L18301 (2009).

Fang, L.H., Wu, J.P., Ding, Z.F., Panza, G.F. High resolution Rayleigh wave group velocity tomography in North China from ambient seismic noise. *Geophys. J. Int.* **181**

(2), 1171-1182 (2010).

Friederich, W., and E. Wielandt. Interpretation of seismic surface waves in regional networks: Joint estimation of wavefield geometry and local phase velocity method and numerical tests, *Geophys. J. Int.* **120**, 731–744 (1995).

Gerstoft, P., Shearer, P.M., Harmon, N., Zhang, J. Global P, PP, and PKP wave microseisms observed from distant storms. *Geophys. Res. Lett.* **35** (23), L23306 (2008).

Gudmundsson, O., Khan, A., Voss, P. Rayleigh-wave group-velocity of the Icelandic crust from correlation of ambient seismic noise. *Geophys. Res. Lett.* **34** (14), L14314 (2007).

Guo, Z., Gao, X., Yao, H.J., Li, J., Wang, W.M. Midcrustal low-velocity layer beneath the central Himalaya and southern Tibet revealed by ambient noise array tomography. *Geochem. Geophys. Geosys.* **10**, Q05007 (2009).

Harmon, N., Forsyth, D., Webb, S. Using ambient seismic noise to determine short-period phase velocities and shallow shear velocities in young oceanic lithosphere. Bull. *Seism. Soc. Am.* **97** (6), 2009-2023 (2007).

Kang, T.S. and Shin, J.S. Surface-wave tomography from ambient seismic noise of accelerograph networks in southern Korea. *Geophys. Res. Lett.* **33** (17, L17303 (2006).

Landes, M., Hubans, F., Shapiro, N. M., Paul, A., Campillo, M. Origin of deep ocean microseisms by using teleseismic body waves. *J. Geophys. Res.-Solid Earth* 115, B05302 (2010).

Langston, C.A. & Liang, C. Gradiometry for polarized seismic waves, *J. Geophys. Res.,* **113**, B08305, doi:10.1029/2007JB005486 (2008).

Li, H.Y., Su, W., Wang, C.Y., Huang, Z.X. Ambient noise Rayleigh wave tomography in western Sichuan and eastern Tibet. *Earth Planet. Sci. Lett.* **282** (1-4): 201-211 (2009).

Li, H.Y., Bernardi, F., Michelini, A. Surface wave dispersion measurements from

ambient seismic noise analysis in Italy. *Geophys. J. Int.* **180** (3), 1242-1252 (2010).

Liang, C.T., and Langston, C.A**.** Ambient seismic noise tomography and structure of eastern North America. *J. Geophys. Res.-Solid Earth* **113** (B3), B03309 (2008).

Lin, F. C., M. H. Ritzwoller, J. Townend, S. Bannister & M. K. Savage. Ambient noise Rayleigh wave tomography of new Zealand. *Geophys. J. Int.,* 170 649-666 (2007).

Lin, F. C., Moschetti, M. P. & Ritzwoller, M. H. Surface wave tomography of the western United States from ambient seismic noise: Rayleigh and Love wave phase velocity maps. *Geophysical Journal International* **173**, 281-298 (2008).

Lin, F., Ritzwoller, M. H. & Snieder, R. Eikonal tomography: surface wave tomography by phase front tracking across a regional broad-band seismic array. *Geophys. J. Int.* **177**, 1091-1110 (2009).

Lin, F.C., M.H. Ritzwoller, Y. Yang, M.P. Moschetti, and M.J. Fouch, The stratification of seismic azimuthal anisotropy in the western US, *Nature Geoscience*, submitted (2010).

Lin, F.C. and M.H. Ritzwoller. Empirically determined finite frequency sensitivity kernels for surface waves, *Geophys. J. Int.*, **182**, 923-932, doi: 10.1111/j.1365-246X.2010.04643.x (2010a).

Lin, F.C. and M.H. Ritzwoller. Eikonal tomography for earthquakes, in preparation (2010b).

Montelli, R., Nolet, G. & Dahlen, F.A. Comment on 'Bananadoughnut kernels and mantle tomography' by van der Hilst and de Hoop, *Geophys. J. Int.,* **167,** 1204–1210 (2006).

Moschetti, M.P., M.H. Ritzwoller, and N.M. Shapiro. Surface wave tomography of the western United States from ambient seismic noise: Rayleigh wave group velocity maps, *Geochem., Geophys., Geosys.*, 8, Q08010, doi:10.1029/2007GC001655 (2007).

Moschetti, M.P., M.H. Ritzwoller, and F.C. Lin, Seismic evidence for widespread crustal deformation caused by extension in the western USA, *Nature*, **464**, N7290, 885-889 (2010a).

Moschetti, M.P., M.H. Ritzwoller, F.C. Lin, and Y. Yang, Crustal shear velocity structure of the western US inferred from ambient noise and earthquake data, *J. Geophys. Res.*, in press (2010b).

Nishida, K., Kawakatsu, H., Obara, K. Three-dimensional crustal S wave velocity structure in Japan using microseismic data recorded by Hi-net tiltmeters. *J. Geophys. Res.-Solid Earth* **113** (B10), B10302 (2008).

Nishida, K., Montagner, J.P., Kawakatsu, H. Global surface wave tomography using seismic hum. *Science* **326** (5949): 112-112 (2009).

Peter, D., Tape, C., Boschi, L. & Woodhouse, J. H. Surface wave tomography: Global membrane waves and adjoint methods, *Geophys. J. Int.*, **171**, 1098–1117 (2007).

Peter, D., Boschi, L. & Woodhouse, J. H. Tomographic resolution of ray and finite frequency methods: a membrane-wave investigation, *Geophys. J. Int.*, **177**, 624–638 (2009).

Pollitz, F.F. Observations and interpretation of fundamental mode Rayleigh wavefields recorded by the Transportable Array (USArray), *Geophys. J. Int.,* **173**, 189-204 (2008).

Prieto, G.A., Lawrence, J. F., and Beroza, G. C. Anelastic Earth structure from the coherency of the ambient seismic field. *J. Geophys. Res. – Solid Earth* **114**, B07303 (2009).

Ritzwoller, M.H., N.M. Shapiro, M.P. Barmin, and A.L. Levshin, Global surface wave diffraction tomography. *J. Geophys. Res.* **107** (B12), 2335 (2002).

Roux, P. ,Sabra, K.G., Gerstoft, P., Kuperman, W.A., Fehler, M.C. P-waves from cross-correlation of seismic noise, *Geophys. Res. Lett.* **32** (19), L19303 (2005).

Sabra, K. G., Gerstoft, P., Roux, P., Kuperman, W. A. & Fehler, M. C. Surface wave tomography from microseisms in Southern California, *Geophys. Res. Lett.* **32**, L14311 (2005).

Saygin, E. & B.L.N. Kennett, Ambient seismic noise tomography of Australian continent. *Tectonophysics,* **481,** 116-125 (2010).

Shapiro, N.M. and Campillo, M. Emergence of broadband Rayleigh waves from correlations of the ambient seismic noise, *Geophys. Res. Lett.,* **31** (7), L07614 (2004).

Shapiro, N.M. and M.H. Ritzwoller. Monte-Carlo inversion for a global shear velocity model of the crust and upper mantle, *Geophys. J. Int.,* 151, 88-105 (2002).

Shapiro, N. M., Campillo, M., Stehly, L. & Ritzwoller, M. H. High-resolution surface-wave tomography from ambient seismic noise. *Science* **307**, 1615-1618 (2005).

Shearer, P. (2009).

Smith, M. L. & Dahlen, F. A. Azimuthal Dependence of Love and Rayleigh-Wave Propagation in a Slightly Anisotropic Medium. *Journal of Geophysical Research* **78**, 3321-3333 (1973).

Stachnik, J.C., Dueker, K., Schutt, D.L.,Yuan, H. Imaging Yellowstone plume-lithosphere interactions from inversion of ballistic and diffusive Rayleigh wave dispersion and crustal thickness data. *Geochem., Geophys., Geosys.* **9**, Q06004 (2008).

Stehly, L., Fry, B., Campillo, M., Shapiro, N.M., Guilbert, J., Boschi, L. Giardini, D. Tomography of the Alpine region from observations of seismic ambient noise. *Geophys. J. Int.* **178** (1), 338-350 (2009).

Sun, X., X. Song, S. Zheng, Y. Yang, M. Ritzwoller, Three dimensional shear velocity structure of crust and upper mantle in China from ambient noise surface wave tomography, *Earthquake Science*, submitted (2010).

Tape, C., Liu, Q., Maggi, A. & Tromp, J. Adjoint tomography of the Southern California crust, *Science*, **325** , 988–992, (2009).

Tromp, J., Tape, C. & Liu, Q. Seismic tomography, adjoint methods, time reversal and banana-doughnut kernels, *Geophys. J. Int.*, **160**, 195–216 (2005).

Tsai, V. C., and M. P. Moschetti. An explicit relationship between time-domain noise correlation and spatial autocorrelation (SPAC) results, *Geophys. J. Int.,* **182**, 454-460, doi:10.1111/j.1365-246X.2010.04633.x (2010).

Van Der Hilst, R.D. & de Hoop, M.V. Banana-doughnut kernels and mantle tomography, *Geophys. J. Int.,* **163,** 956–961, 2005.

Villaseñor, A., Y. Yang, M. H. Ritzwoller & J. Gallart. Ambient noise surface wave tomography of the Iberian Peninsula: Implications for shallow seismic structure. *Geophys. Res. Lett.* ***34***, L11304, doi:10.1029/2007GL030164 (2007).

Wielandt, E. Propagation and structural interpretation of non-plane waves, *Geophys. J. Int.* **113**, 45– 53 (1993).

Yang, Y.J. & Forsyth D.W. Regional tomographic inversion of the amplitude and phase of Rayleigh waves with 2-D sensitivity kernels, *Geophys. J. Int.,* **166**, 1148-1160 (2006).

Yang, Y.J., Ritzwoller, M.H., Levshin, A.L., Shapiro, N.M. Ambient noise Rayleigh wave tomography across Europe. *Geophys. J. Int.* **168** (1): 259-274 (2007).

Yang, Y. J., A. B. Li & M. H. Ritzwoller. Crustal and uppermost mantle structure in southern Africa revealed from ambient noise and teleseismic tomography. *Geophys. J. Int.,* 174**,** 235-248 (2008a).

Yang, Y., Ritzwoller, M. H., Lin, F. -C., Moschetti, M. P. & Shapiro, N. M. Structure of the crust and uppermost mantle beneath the western United States revealed by ambient noise and earthquake tomography. *J. Geophys. Res. -Solid Earth* **113**, B12310 (2008b).

Yang, Y. and M.H. Ritzwoller, Teleseismic surface wave tomography in the western US using the Transportable Array component of USArray, *Geophys. Res. Letts.*, **5**, L04308, doi:10.1029/2007GL032278 (2008c).

Yang, Y., et al., Rayleigh wave phase velocity maps of Tibet and the surrounding regions from ambient seismic noise tomography, *Geochem., Geophys., Geosys.*, **11** (8), Q08010, doi:10.1029/2010GC003119 (2010).

Yao, H.J. , van der Hilst, R.D., de Hoop, M.V. Surface-wave array tomography in SE Tibet from ambient seismic noise and two-station analysis - I. Phase velocity maps. *Geophys. J. Int.,* 1**66** (2), 732-744 (2006).

Yao, H.J., Beghein, C., and van der Hilst, R.D. Surface wave array tomography in SE Tibet from ambient seismic noise and two-station analysis - II. Crustal and upper-mantle structure, *Geophys. J. Int.* **173** (1), 205-219 (2008).

Yao H., Campman, X., de Hoop, M.V., van der Hilst, R.D. Estimation of surface-wave Green's function from correlations of direct waves, coda waves, and ambient noise in SE Tibet, *Phys. Earth Planet. Int.,* doi:10.1016/j.pepi.2009.07.002 (2009).

Yao, H., van der Hilst, R.D., and Montagner J.-P. Heterogeneity and anisotropy of the lithosphere of SE Tibet from surface wave array tomography*, J. Geophys. Res.,* doi:10.1029/2009JB007142, in press (2010).

Yoshizawa,K. & Kennett, B.L.N. Determination of the influence zone for surface wave paths, *Geophys. J. Int.,* **149,** 441–454 (2002).

Zhan, Z.W., Ni, S.D., Helmberger, D.V., Clayton, R.W. Retrieval of Moho-reflected shear wave arrivals from ambient seismic noise. *Geophys. J. Int.* **182** (1), 408-420 (2010).

Zheng, S. H., X. L. Sun, X. D. Song, Y. J. Yang & M. H. Ritzwoller. Surface wave tomography of China from ambient seismic noise correlation. *Geochem. Geophys. Geosyst.*, *9*, Q05020, doi:10.1029/2008GC001981 (2008).

Zheng, X.F., Jiao, W.J., Zhang, C.H., Wang, L.S. Short-period Rayleigh-wave group velocity tomography through ambient noise cross-correlation in Xinjiang, Northwest China. *Bull. Seism. Soc. Am.* **100** (3), 1350-1355 (2010a).

Zheng, Y., Y. Yang, M.H. Ritzwoller, X. Zheng, X. Xiong, Z. Li, Crustal structure of the northeastern Tibetan Plateau, the Ordos Block and the Sichuan Basin from ambient noise tomography, *Earthquake Science*, submitted (2010b).

Figure Captions:

Figure 1. There are 1021 EarthScope USArray Transportable Array and Permanent Array stations (black triangles) used in this study. Locations of geographical points for data results presented later in the paper are shown with stars, red contours denote tectonic regions, and the yellow rectangle outline the location of the results shown in Fig. 11.

Figure 2. The 24 sec Rayleigh wave phase travel time surface computed from ambient noise empirical Green's functions across the western US based on central station (USArray, Transportable Array) Q16A in Utah. Travel time lines are presented in increments of wave period. Map is truncated within two wavelengths of the station and where the travel times are not well determined. Station Q16A operated simultaneously with the 843 stations shown, but only for a short time near the western and eastern boundaries of the map.

Figure 3. The local (a) phase speed and (b) ray direction inferred from the gradient of the 24 sec period Rayleigh wave travel time map shown in Fig. 2 for central TA station Q16A. In (b), the difference between the observed and radial directions is shown with the background color.

Figure 4. Phase speeds as a function of azimuthal angle and averaged in each 20° bin for the 24 sec Rayleigh wave are plotted as 1σ (standard deviation) error bars for example points in (a) Nevada (242°E, 42°N) and (b) Arizona (250°E, 36°N), identified with stars in Fig. 1. The best-fitting 2ψ curve (eqn. (3)) is presented as the green line in each panel. Estimated values of c_o', A and ϕ are listed at upper left in each panel. The 2ψ component of anisotropy is clear in both panels.

Figure 5. (a) The 24 sec Rayleigh wave isotropic phase speed map taken from ambient noise by averaging all local phase speed measurements at each point on the map. (b) The amplitudes and fast directions of the 2ψ component of the 24 sec Rayleigh wave phase velocities. The amplitude of anisotropy is identified with the length of the bars, which point in the fast axis direction, and is color-coded in the background. At 24 sec period, Rayleigh wave anisotropy reflects conditions in a mixture of the crust and uppermost mantle.

Figure 6. Uncertainties in (a) the isotropic Rayleigh wave phase speed in m/s, (b) the 2ψ fast axis direction in degrees, and (c) the amplitude of the 2ψ component of anisotropy (in m/s) for the 24 sec Rayleigh wave. Uncertainties are estimated at each point based on the scatter of measurements over azimuth and by fitting equation (3) to results such as those shown in Fig. 4.

Figure 7. (a) & (b) Isotropic maps of the 10 sec and 30 sec period Rayleigh wave phase speed observed via eikonal tomography applied to ambient noise by averaging all measurements at each location, similar to Fig. 5a. (d) & (e) Azimuthal anisotropy from ambient noise also at 10 sec and 30 sec period, similar to Fig. 5b. (c) &(f) Maps of the isotropic Rayleigh wave speed and azimuthal anisotropy at 30 sec period observed from teleseismic earthquakes via eikonal tomography (Lin and Ritzwoller, 2010b), presented for comparison with (b) and (e).

Figure 8. Isotropic and azimuthally anisotropic dispersion curves in northern Nevada, shown with a star in Fig. 1. Only ambient noise measurements are used at periods below 25 sec, ambient noise and earthquake measurements are averaged between 25 sec and 45 sec period, and only earthquake measurements are used above 45 sec period. Phase velocity is presented in km/s, anisotropy amplitude in percent, and the fast direction of

anisotropy in degrees east of north. Measurement uncertainties are presented with 1 standard deviation error bars. Additional scaling as described in Lin et al. (2010) is applied on the uncertainties of anisotropy measurements based on the misfit to the data by eqn. (3). The best-fitting curves based on the isotropic and anisotropic inversions are presented as the green line in each panel.

Figure 9. 3D model results: (a) Isotropic Vs velocity in the crust, (b) isotropic Vs velocity in the uppermost mantle, (c) azimuthal anisotropy in the middle to lower crust, and (d) anisotropy in the uppermost mantle. Results are taken from the model of Lin et al. (2010).

Figure 10. Rayleigh wave phase speeds determined from ambient noise as a function of azimuthal angle and averaged in each 20° azimuthal bin are plotted as 1σ (standard deviation) error bars at periods of 10 sec, 30 sec, and 60 sec for the point in northern Utah shown with a star in Fig. 1. The green dashed line is the best fitting 1ψ and 2ψ curve. The 1ψ component is small at periods below ~40 sec, but dominates the azimuthal dependence of phase velocities at 60 sec period. The 1ψ component is spurious, resulting from the apparent phase velocity increase or decrease caused by wavefront healing.

Figure 11. (a)-(c) Maps of isotropic Rayleigh wave speeds at 10 sec, 30 sec, and 60 sec period (presented in km/s) determined from ambient noise where the orientation of the 1ψ component of Rayleigh phase speed is over-plotted with an arrow pointing in the fast-direction. Arrows are plotted only if the peak-to-peak amplitude of the 1ψ component is at least 2%. At 60 sec, arrows point away from slow isotropic anomalies and toward fast anomalies. (d)-(f) Amplitude of the 1ψ component of phase speed, presented in percent. Strong amplitudes surround the principal isotropic anomalies at 60 sec period.

Figure 12. (a) The 20 sec period Rayleigh wave empirical finite frequency kernel for the USArray station pair L04A-GSC. The A-B dashed line indicates the mid-distance cross section shown in (c). (b) Same as (a), but the analytical kernel is shown. (c) The mid-distance cross section of the sensitivity kernels shown in (a) and (b). (d)-(f) Same as (a)-(c), but for the 40 sec period Rayleigh wave.

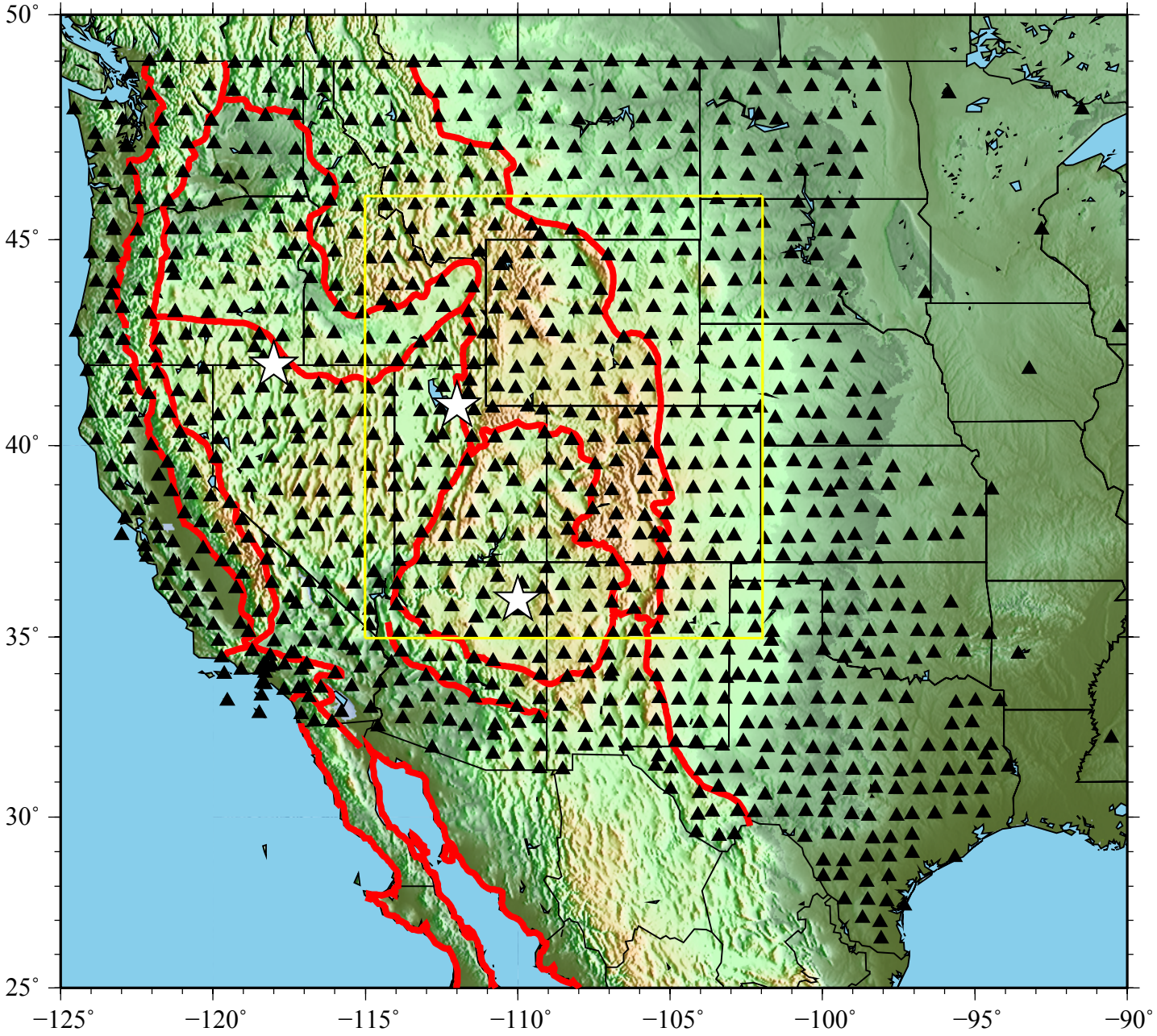

Figure 1

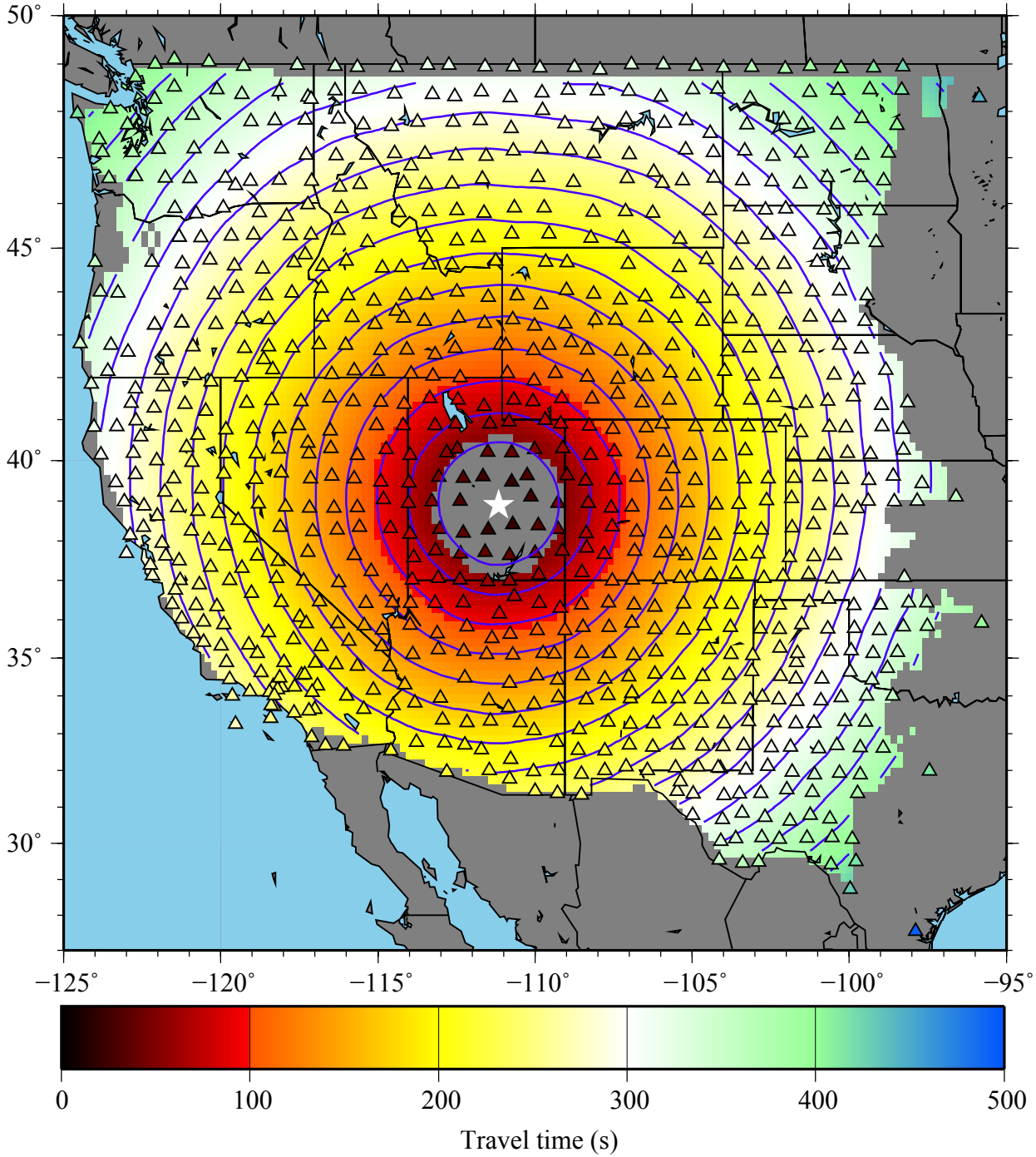
50°
45°
40°
35°
30°
−125°
−120°
−115°
−110°
−105°
−100°
−95°
0
100
200
300
400
500
Travel time (s)

Figure 2

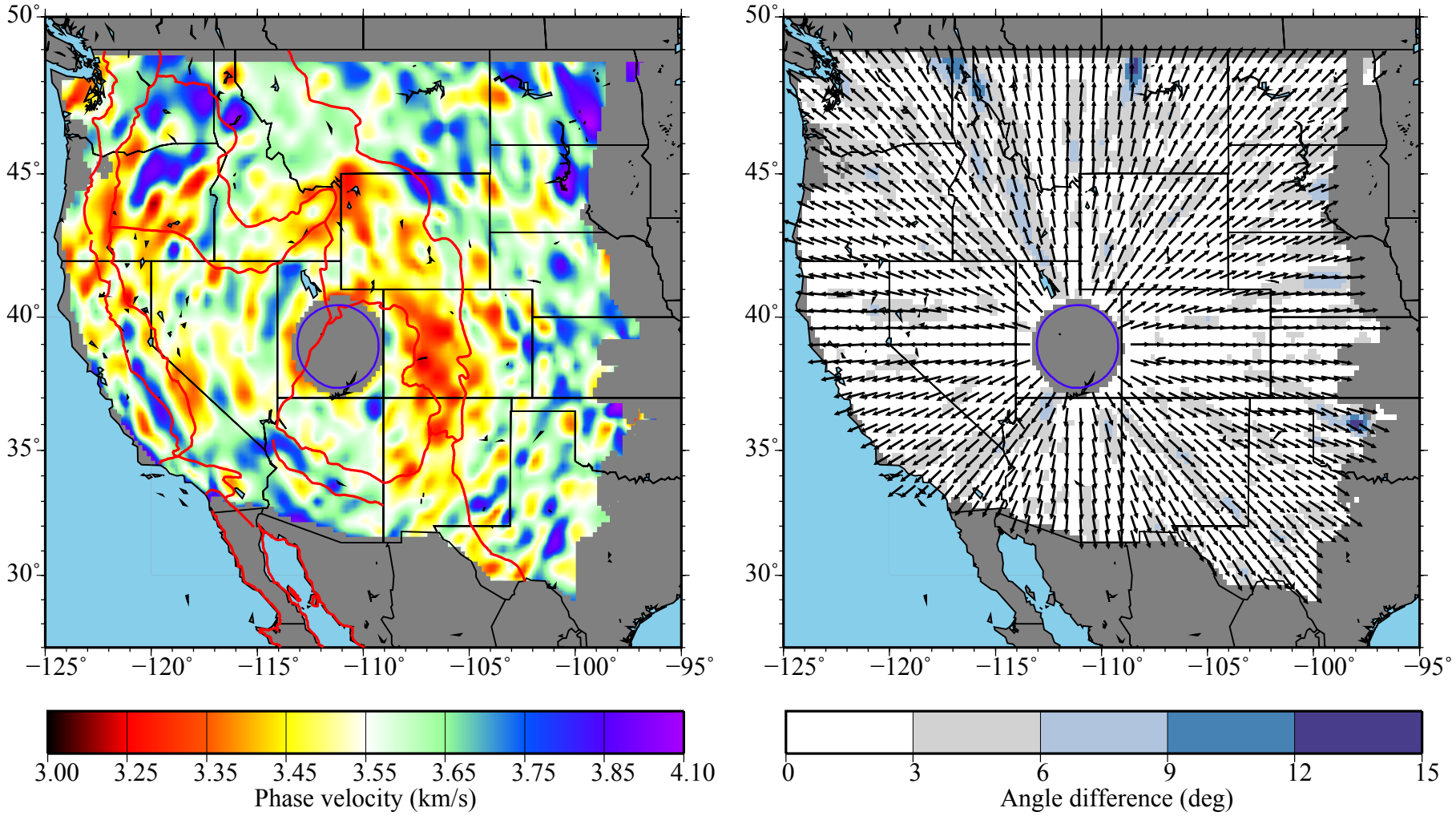
50°
45°
40°
35°
30°
−125°
−120°
−115°
−110°
−105°
−100°
−95°
3.00
3.25
3.35
3.45
3.55
3.65
3.75
3.85
4.10
Phase velocity (km/s)
0
3
6
9
12
15
Angle difference (deg)

Figure 3

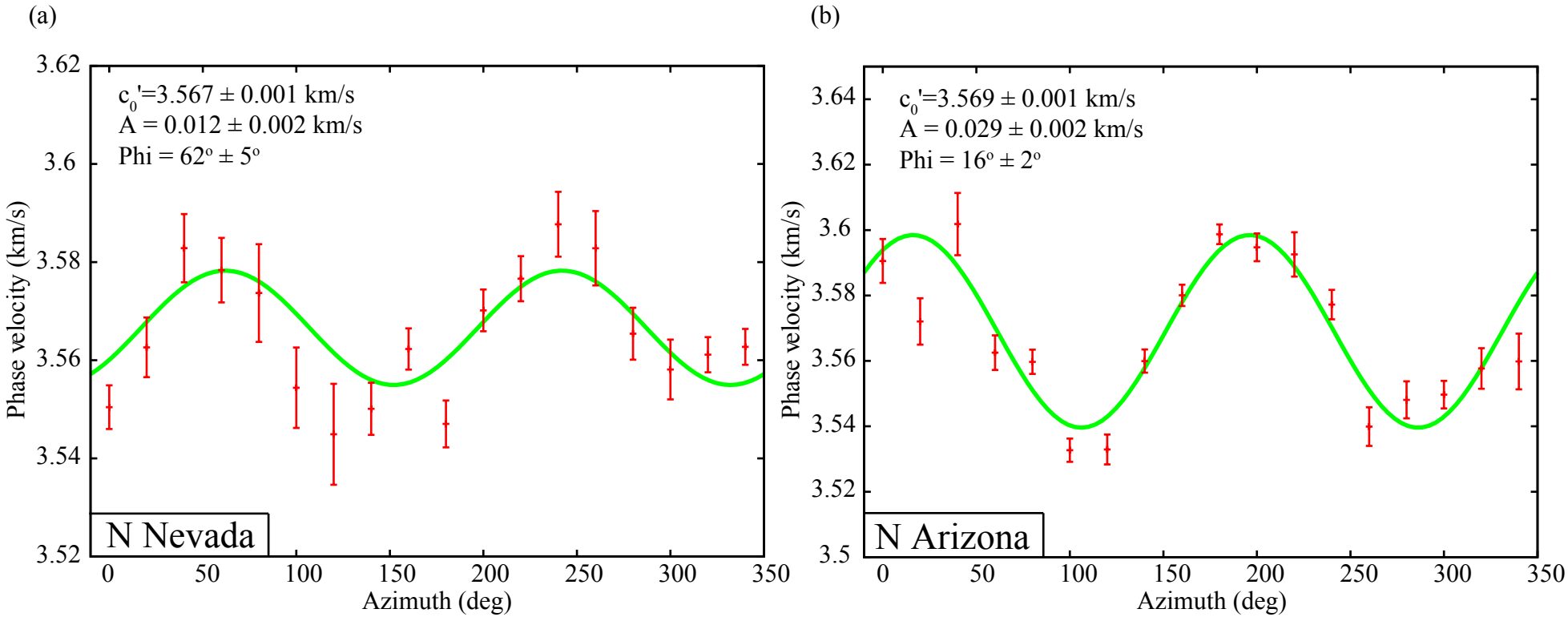
(a)
c0'=3.567 ± 0.001 km/s
A = 0.012 ± 0.002 km/s
Phi = 62° ± 5°
N Nevada
Phase velocity (km/s)
Azimuth (deg)
3.62
3.6
3.58
3.56
3.54
3.52
0
50
100
150
200
250
300
350
(b)
c0'=3.569 ± 0.001 km/s
A = 0.029 ± 0.002 km/s
Phi = 16° ± 2°
N Arizona
Phase velocity (km/s)
Azimuth (deg)
3.64
3.62
3.6
3.58
3.56
3.54
3.52
3.5

Figure 4

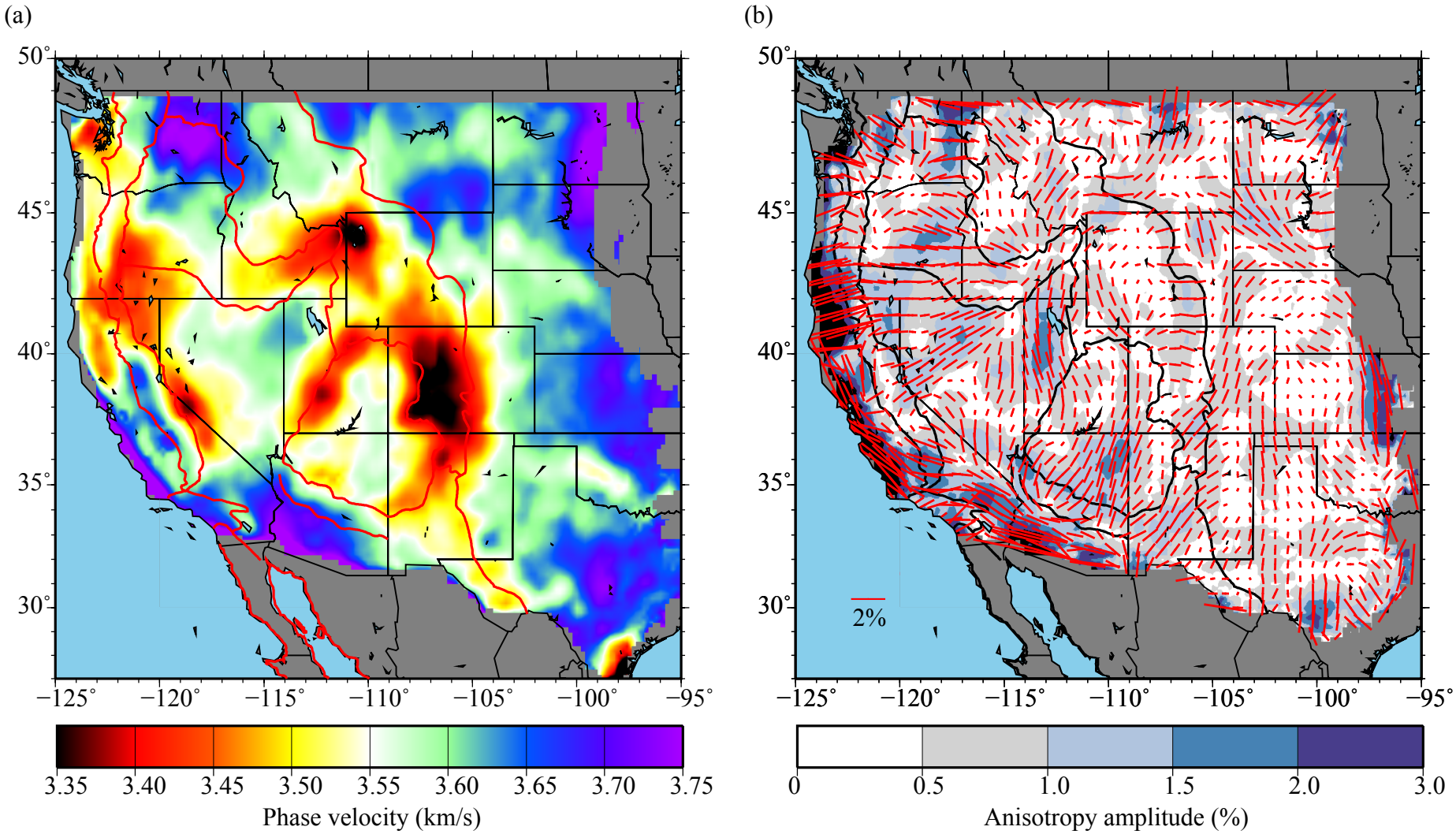
(a)
(b)
50°
45°
40°
35°
30°
−125°
−120°
−115°
−110°
−105°
−100°
−95°
3.35
3.40
3.45
3.50
3.55
3.60
3.65
3.70
3.75
Phase velocity (km/s)
2%
0
0.5
1.0
1.5
2.0
3.0
Anisotropy amplitude (%)

Figure 5

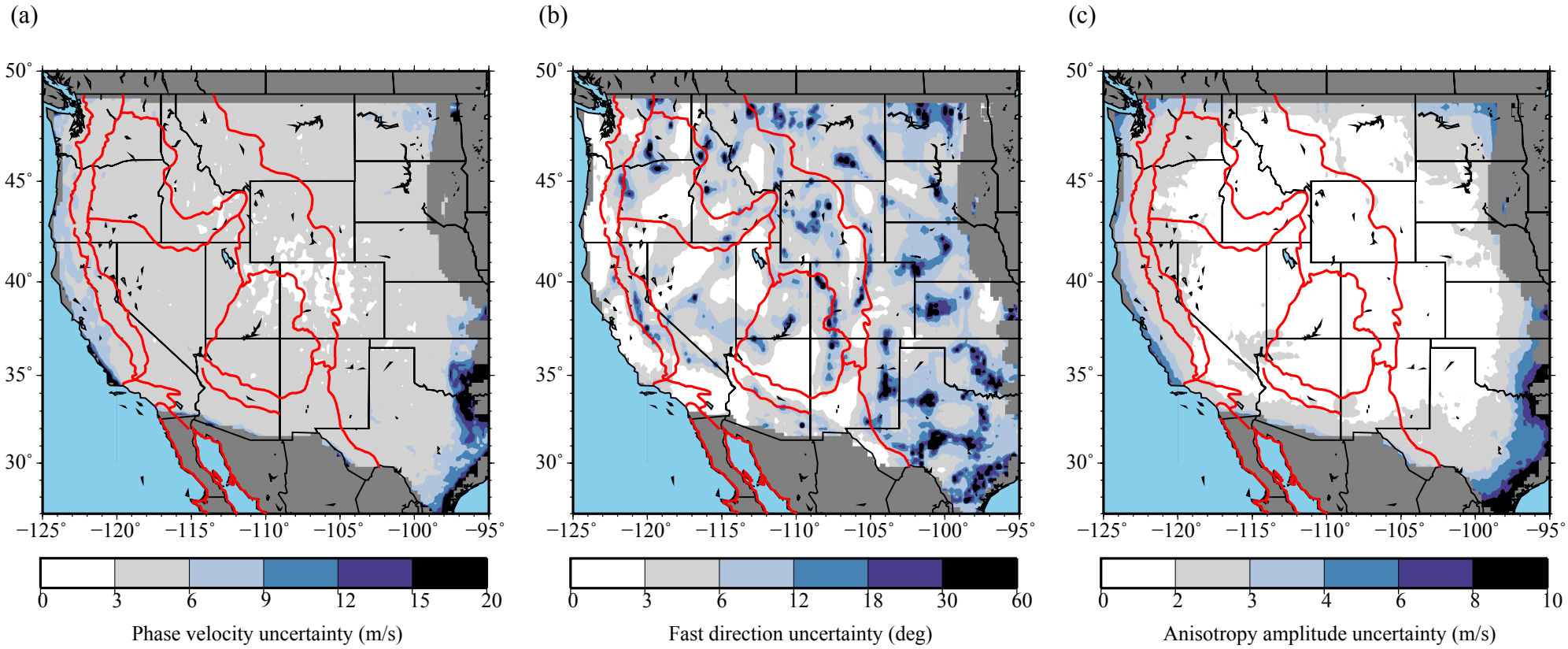
(a)
(b)
(c)
50°
45°
40°
35°
30°
−125°
−120°
−115°
−110°
−105°
−100°
−95°
0
3
6
9
12
15
20
Phase velocity uncertainty (m/s)
0
3
6
12
18
30
60
Fast direction uncertainty (deg)
0
2
3
4
6
8
10
Anisotropy amplitude uncertainty (m/s)

Figure 6

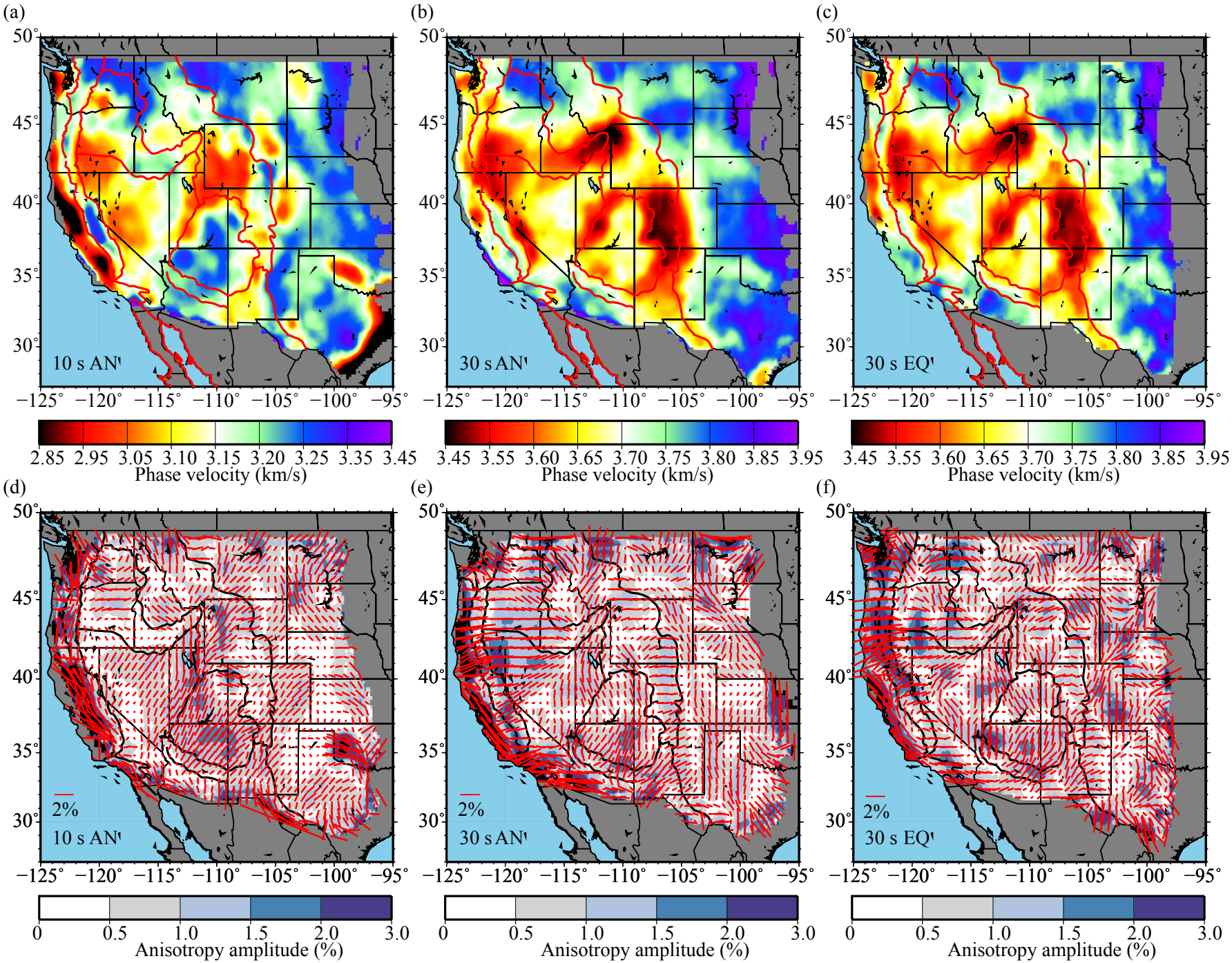
(a)
(b)
(c)
10 s ANT
30 s ANT
30 s EQT
50°
45°
40°
35°
30°
−125° −120° −115° −110° −105° −100° −95°
2.85 2.95 3.05 3.10 3.15 3.20 3.25 3.35 3.45
3.45 3.55 3.60 3.65 3.70 3.75 3.80 3.85 3.95
Phase velocity (km/s)
(d)
(e)
(f)
2%
0 0.5 1.0 1.5 2.0 3.0
Anisotropy amplitude (%)

Figure 7

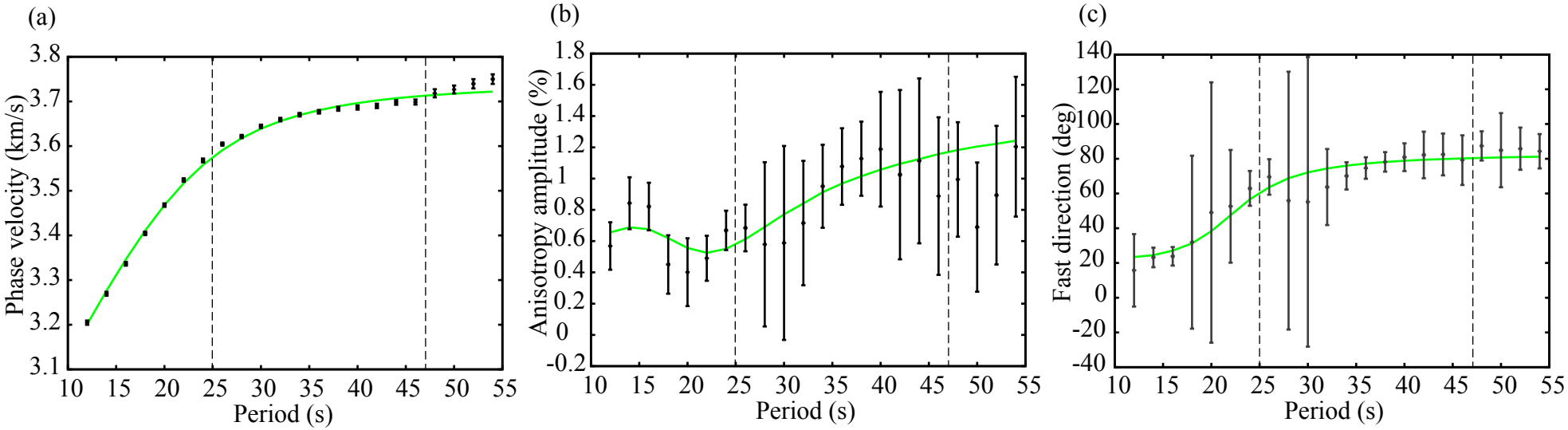
(a)
Phase velocity (km/s)
3.8
3.7
3.6
3.5
3.4
3.3
3.2
3.1
10 15 20 25 30 35 40 45 50 55
Period (s)
(b)
Anisotropy amplitude (%)
1.8
1.6
1.4
1.2
1
0.8
0.6
0.4
0.2
0
-0.2
10 15 20 25 30 35 40 45 50 55
Period (s)
(c)
Fast direction (deg)
140
120
100
80
60
40
20
0
-20
-40
10 15 20 25 30 35 40 45 50 55
Period (s)

Figure 8

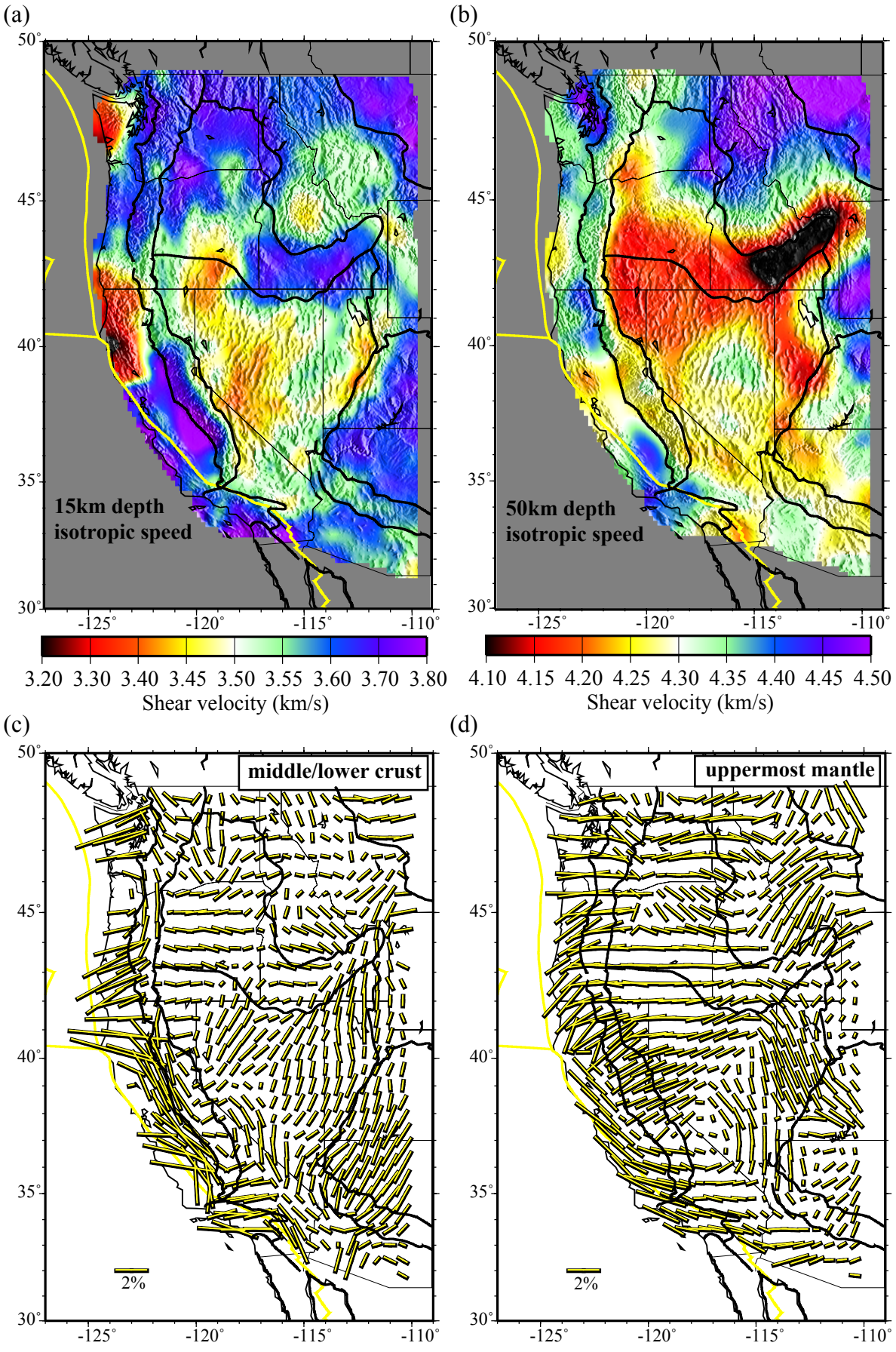
(a)
(b)
(c)
(d)
15km depth
isotropic speed
50km depth
isotropic speed
middle/lower crust
uppermost mantle
2%
2%
50°
45°
40°
35°
30°
-125°
-120°
-115°
-110°
3.20 3.30 3.40 3.45 3.50 3.55 3.60 3.70 3.80
Shear velocity (km/s)
4.10 4.15 4.20 4.25 4.30 4.35 4.40 4.45 4.50
Shear velocity (km/s)

Figure 9

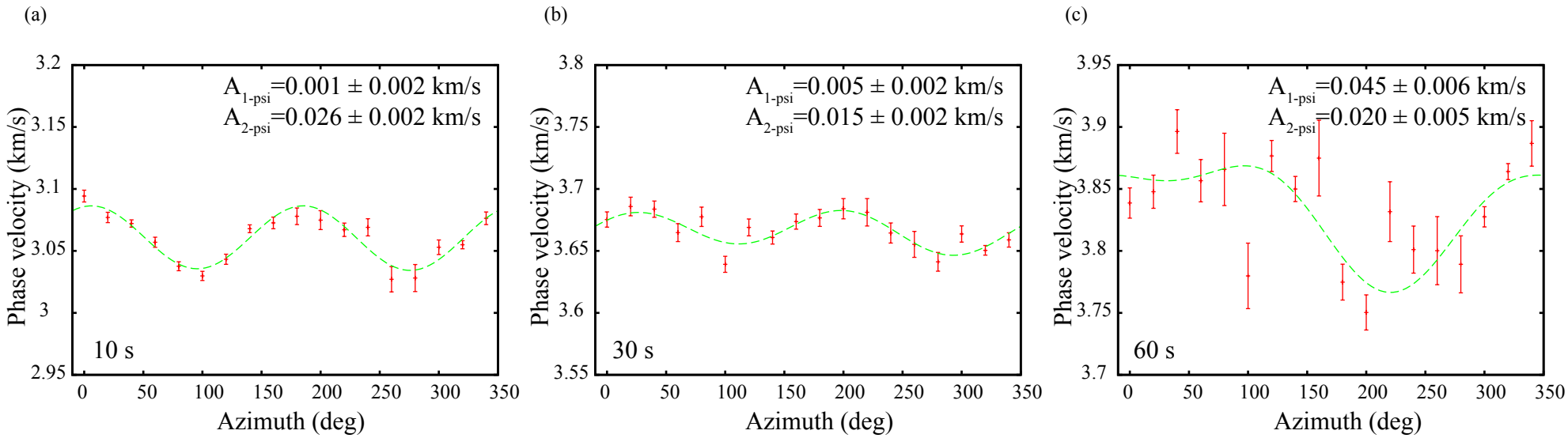
(a)
(b)
(c)
A1-psi=0.001 ± 0.002 km/s
A2-psi=0.026 ± 0.002 km/s
A1-psi=0.005 ± 0.002 km/s
A2-psi=0.015 ± 0.002 km/s
A1-psi=0.045 ± 0.006 km/s
A2-psi=0.020 ± 0.005 km/s
10 s
30 s
60 s
Phase velocity (km/s)
Azimuth (deg)

Figure 10

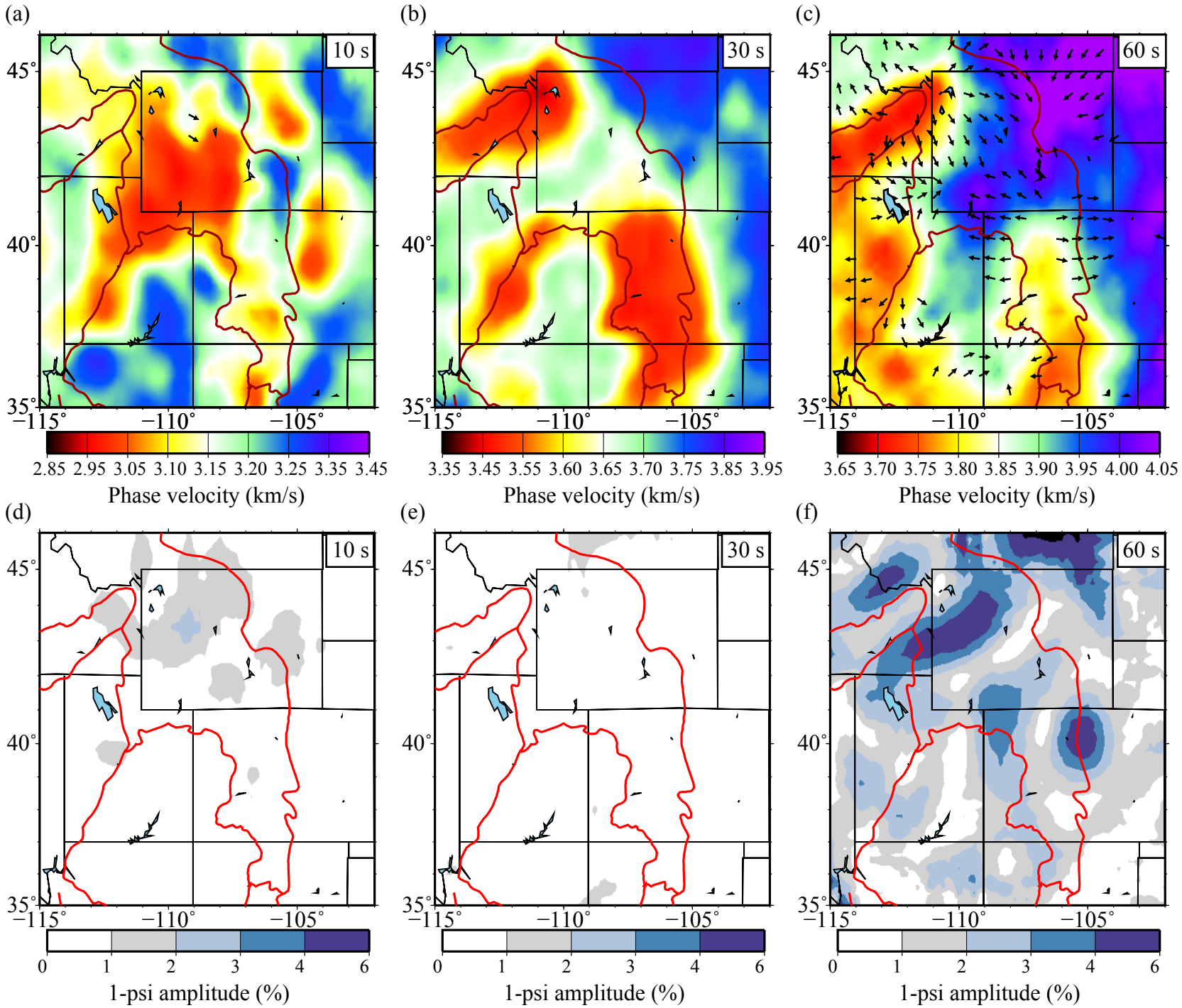
(a)
10 s
45°
40°
35°
−115°
−110°
−105°
2.85 2.95 3.05 3.10 3.15 3.20 3.25 3.35 3.45
Phase velocity (km/s)
(b)
30 s
3.35 3.45 3.55 3.60 3.65 3.70 3.75 3.85 3.95
Phase velocity (km/s)
(c)
60 s
3.65 3.70 3.75 3.80 3.85 3.90 3.95 4.00 4.05
Phase velocity (km/s)
(d)
10 s
0 1 2 3 4 6
1-psi amplitude (%)
(e)
30 s
1-psi amplitude (%)
(f)
60 s
1-psi amplitude (%)

Figure 11

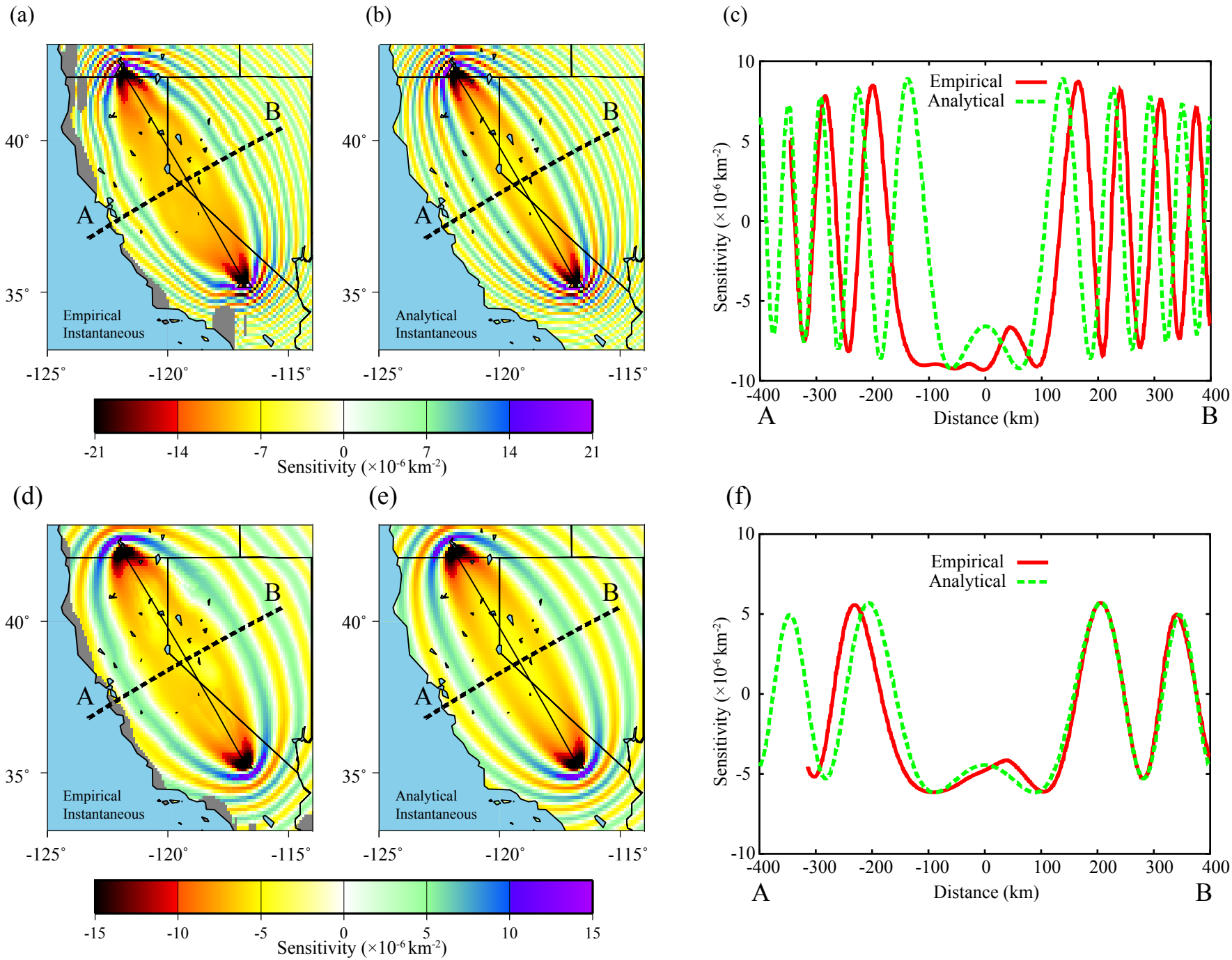
(a)
(b)
(c)
(d)
(e)
(f)
A
B
40°
35°
-125°
-120°
-115°
Empirical
Instantaneous
Analytical
Instantaneous
-21
-14
-7
0
7
14
21
Sensitivity (×10⁻⁶ km⁻²)
-15
-10
-5
0
5
10
15
Empirical
Analytical
Sensitivity (×10⁻⁶ km⁻²)
Distance (km)
-400
-300
-200
-100
0
100
200
300
400

Figure 12